J. Fluid Mech. (2014), *vol.* 747, *pp.* 103–118.
doi:10.1017/jfm.2014.108

Bridging local to global dynamics of drop impact onto solid substrates

H. Lastakowski, F. Boyer, A.-L. Biance†, C. Pirat and C. Ybert

Institut Lumière Matière, University Lyon 1 – CNRS, UMR 5306, Université de Lyon, 69622 Villeurbanne CEDEX, France

(Received 11 June 2013; revised 17 December 2013; accepted 22 February 2014; first published online 14 April 2014)

The shape of impacting drops onto a solid surface is investigated by probing the local flow velocity and the local thickness profile of the spreading lamella during the drop impact. First, as a model situation of no viscous coupling between the liquid and the substrate, the impact of a drop onto hot plates, above the Leidenfrost temperature, is considered. In this case, we demonstrate that the velocity and thickness profiles are in good agreement with inviscid convective flow theory. This local description allows us to revisit the modelling of well-studied global behaviour such as drop spreading. Building from this idealized situation, viscous boundary-layer effects emerging from frictional coupling on a cold surface are then captured.

Key words: capillary flows, drops, interfacial flows

1. Introduction

Drop impact onto a dry solid substrate is a ubiquitous phenomenon encountered in many everyday life and industrial situations ranging from inkjet printing to pesticide delivery and to spray cooling as depicted by Yarin (2006). Although pioneering investigations can be traced back to more than a century ago by Worthington (1876), a detailed understanding of what controls the rich possibilities of the impact's outcome remains elusive. Most of the studies to date have focused on global parameters such as the splash threshold (Wachters & Westerling 1966; Range & Feuillebois 1998; Bussmann, Chandra & Mostaghimi 2000), contact time (Richard, Clanet & Quere 2002), maximal extension (Chandra & Avedisian 1991; Clanet *et al.* 2004) or bouncing restitution coefficient (Biance *et al.* 2006). This has led to the identification of many different scenarios concerning spreading, deposition, recoil and bouncing, various forms of splashing and fragmentation that depend on many control parameters including surface roughness, wettability and ambient gas pressure (Xu, Zhang & Nagel 2005; Xu 2007; Latka *et al.* 2012). However, moving toward a comprehensive understanding of the impact dynamics now requires quantitative investigations at a more local scale. This has been exemplified recently by the experimental efforts (Driscoll & Nagel 2011; de Ruiter *et al.* 2012; Kolinski *et al.* 2012; van der Veen *et al.* 2012) devoted to measuring the dynamics of the intercalated air film present during the first steps of the impact, as it happens to be crucial in the splash process (Xu *et al.* 2005; Mandre, Mani & Brenner 2009). Beyond air film description, rim dynamics and

† Email address for correspondence: anne-laure.biance@univ-lyon1.fr

subsequent splash events directly depend on local characteristics of liquid spreading flow. Detailed inputs from the lamella flow have been absent so far from the different global balance models performed (Chandra & Avedisian 1991; Clanet *et al.* 2004; Biance *et al.* 2006) which, in the end, failed to identify unambiguously relevant physical ingredients. In the present study, we propose an experimental characterization of the liquid flow, both velocity and thickness profiles, upon impact and spreading of drops. We particularly focus on impacts over superheated substrates, for which a Leidenfrost effect occurs (Wachters & Westerling 1966; Chandra & Avedisian 1991; Biance, Clanet & Quere 2003; Biance *et al.* 2006).

Beyond the practical interest of such situations for thermal transfer and cooling processes, as described by Wachters & Westerling (1966), the appearance of an intercalated vapour layer also constitutes a *mechanical* insulator. Indeed it essentially prevents any frictional coupling between the liquid and the underlying solid substrate. As such, drop impact on hot plates constitutes a model configuration where liquid dynamics reduces to inviscid flow contributions, a reference situation from which additional contributions can be built on. This combination of new quantitative information on local lamella hydrodynamics and model frictionless situation allows to compare and discriminate among the different theoretical descriptions recently proposed by Roisman, Berberovic & Tropea (2009), Eggers *et al.* (2010) and Villermaux & Bossa (2011). This local description constitutes the prerequisite building block to bridge to classically examined global features such as the maximum spreading radius. Combining our measured flow description with rim dynamic modelling indeed allows us to reproduce global experimental data such as the maximal drop extension or timescale to reach this maximum, going beyond existing scaling laws based on previous global balances. Finally, this investigation in a Leidenfrost situation also constitutes a reference starting configuration towards the comprehension of more complex situations. As a first example, the case of additional friction is investigated by considering the impact on the same smooth but cold substrate. Here, the flow perturbation due to additional friction can be directly captured experimentally.

2. Experiments

Drops of different liquids (ethanol, isopropanol–glycerol mixtures) are released from a needle to impact onto a smooth silicon wafer deposited on a hot plate. Impacts are recorded from the top view via a high-speed camera (Photron SA-4) at up to 30 000 f.p.s. The camera is placed at an angle of 20° from the vertical direction and receives specular reflexion of the light on the wafer or the drop. Overall, drop radii R and kinematic viscosities ν are varied in the range 0.8–1.8 mm and 1–32 mm^2 s^{-1}, respectively, while impact velocities U, set by the free fall height, lie between 1 and 4 m s^{-1}. The dimensionless parameters associated with the impact process are the Reynolds Re and the Weber We numbers defined as $Re = (UR)/\nu$ and $We = (\rho U^2 R)/\gamma$ with ρ and γ the liquid density and surface tension, respectively. The present study focuses on inertia-dominated regimes with Re (respectively, We) varied from 20 to 5600 (respectively, 20 to 1100). Figure 1(*a*) shows a typical chronophotograph of the global-scale drop impact on a superheated surface: spreading and rim formation, droplet emission and recoil.

To access local information on lamella dynamics, a flow profile is obtained by adding iriodin particles (Merck 111 rutile fine satin, $r_p = 5$ μm, $\rho_p = 3300 \pm 10$ kg m^{-3}) to the drop and carrying out particle image velocimetry (PIV) analysis as shown in figure 1(*d*). The time scale at which the particles will follow the liquid

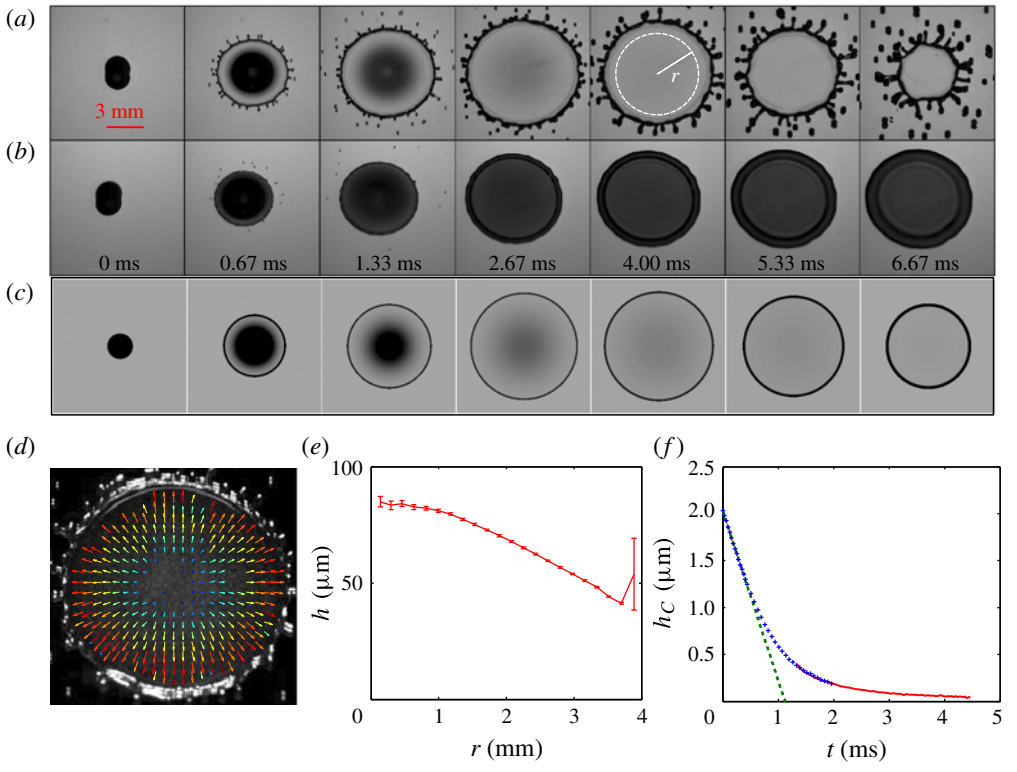

FIGURE 1. (Colour online) (*a*)–(*c*) Image sequence of the impact of an ethanol drop ($R = 1.1$ mm, $U = 2$ m s^{-1}) on a silicon wafer. (*a*) Leidenfrost impact on a plate heated at 350 °C. (*b*) Impact at room temperature. (*c*) Numerical predictions referring to (3.3), (3.4) and (3.5) performed with Matlab for the same conditions as (*a*). The lamella in (*b*) appears darker showing that its thickness is larger in the case of room-temperature impact. (*d*) Velocity field inside an impacting Leidenfrost drop obtained by PIV measurements ($t = 4$ ms). The arrow length indicates the horizontal velocity magnitude. (*e*) Thickness h profile along the radial coordinate r at $t = 4$ ms. The rim is located at $r = 4.4$ mm. (*f*) Central thickness versus time (crosses (blue online), side view; full line (red online), top view; dashed line (green online), $2R - Ut$). Experiments (*d–f*) correspond to the impact of an ethanol drop of initial radius $R = 1.02$ mm and of initial velocity $U = 1.8$ m s^{-1}.

movement is given by a balance between viscous drag and inertia and reads as $T = (2/9)((\rho_p - \rho_l)/\eta)r^2$. Its value is of the order of 1 μs, largely below a typical timescale for flow variations in the regime explored experimentally, which reads as $\tau = R/U > 200$ μs. Note also that the flow velocity profiles accessible here are not resolved in the vertical direction and are consequently averaged along the local lamella thickness.

The local thickness $h(r, t)$ of the spreading liquid lamella, usually inaccessible due to an external rim at the edge of the drop, is measured using light absorption, with a dye (Eriochrome black *T*, Acros organics) being added to the liquid. Grey-level intensities of light are associated with solution thicknesses through a Beer–Lambert law calibrated on controlled thickness liquid pools. Circularly averaged lamella height profiles can be constructed at different times after impact, such as that reported in figure 1(*e*). The accuracy and limitations of this technique are discussed in a dedicated

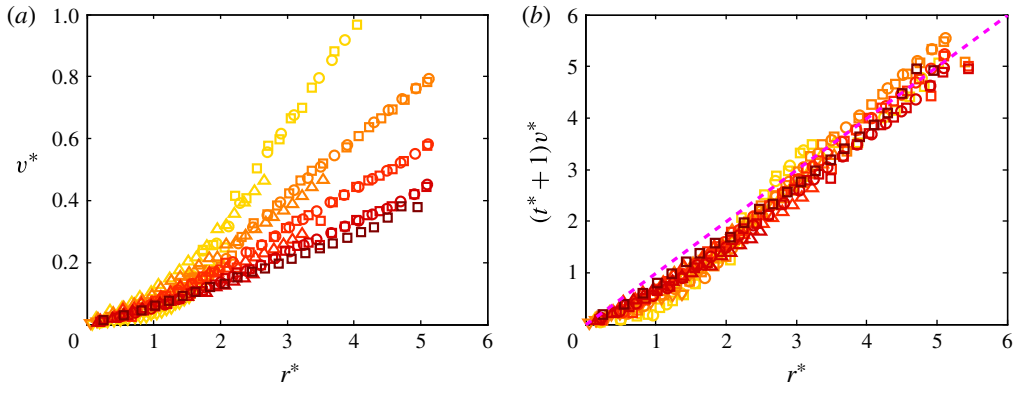

FIGURE 2. (Colour online) (*a*) Normalized velocity $v^* = v/U$ as a function of the position in the radial coordinate in the drop $r^* = r/R$ at different times ($t^* = tU/R = 4, 6, 8, 10$ and 12) and different impact velocities (□, $U = 4$ m s^{-1}; ○, $U = 3$ m s^{-1}; △, $U = 2$ m s^{-1}; ▽, $U = 1$ m s^{-1}) for Leidenfrost ethanol drop impacts with $R = 1.2$ mm. (*b*) Normalized velocity v^* times $(t^* + 1)$ as a function of the position in the radial coordinate in the drop r^* (same data as in (*a*)). The dashed line has a slope of 1.

appendix. Finally, note that both iriodin and dye additions were checked to leave global impact dynamics unchanged.

3. Leidenfrost impacts

We first focus on the impact dynamics onto superheated surfaces, for which frictional coupling with the substrate is minimized. We start with a complete local characterization of impact shape, and then move to the global dynamic description.

3.1. *Local characterization*

In figure 2(*a*) we report the measured radial velocity fields at various times and impact velocities, with dimensionless position, velocity and time defined as $r^* = r/R$, $v^* = v/U$ and $t^* = t/\tau$, where $\tau = R/U$. For radii larger than $r^* = 2$, all velocity profiles appear to depend approximately linearly on r^*, with a time-dependent slope. Deviations from this linear dependance can be observed at short times t^* or small radius r^*, underlying the limitations of the asymptotic regime of large t^* and large r^*. Furthermore, the inverse of this slope is found to vary linearly with time with a delay of order τ so that all experimental velocity data collapse when plotted against $r^*/(t^* + \alpha)$, with α equal to one, as shown in figure 2(*b*).

The dynamic characterization of these impacts on superheated surfaces is pursued by measuring the lamella thickness evolution, an instantaneous profile being shown in figure 1(*e*). The thickness decreases along the radial coordinate, the maximal thickness being reached at the centre of the drop. Focusing on the central lamella thickness h_c, the time evolution of h_c is reported in the inset of figure 3(*a*) for different drop radii R and impact velocities U. In the previously defined reduced coordinates, with lengths normalized by R and time by τ, all data collapse on a single master curve as reported in figure 3(*a*). This decrease represented here on a log–log scale is in good agreement with $h_c^* \propto (t^* + 1)^{-2}$ and with the theoretical predictions as shown in the following.

Both velocity profile and drop height evolution can be rationalized considering the inviscid flow limit, which is legitimated here both by the high Re and the absence

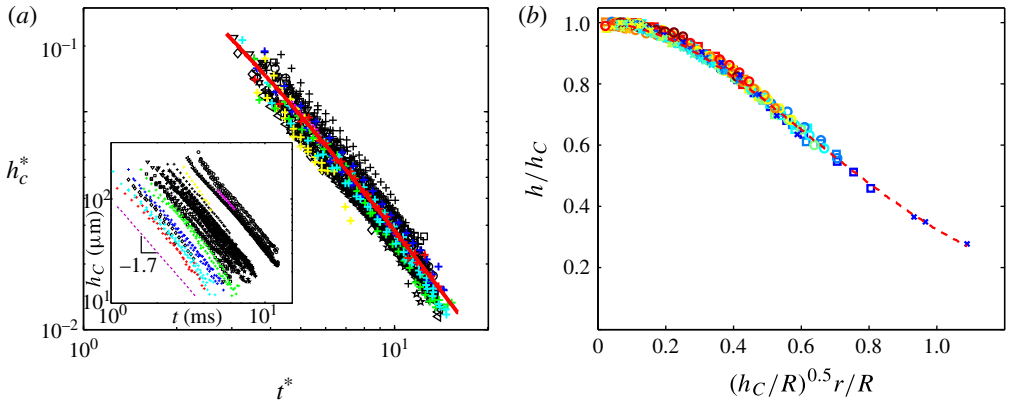

FIGURE 3. (Colour online) (*a*) Dimensionless central thickness $h^* = h/R$ versus the dimensionless time $t^* = (tU)/R$ for various Leidenfrost impacts. The thick line (shown in red online) is a fit of the data satisfying $h^* = 3.19/((t^* + 1)^2)$, given by (3.3). In inset represents the central thickness variations in physical units h (μm), t (ms). (*b*) Rescaled thickness profiles at different times for Leidenfrost impacts of ethanol drops. Initial drop radii vary from 0.8 to 1.8 mm, impact velocity varies from 1 to 4 m s^{-1}. Profiles are shown for different times after $t^* \geqslant 4$. The dashed line shows a fit given by (3.4).

of friction owing to the Leidenfrost effect. This problem is reminiscent of the remote asymptotic solution in thin films as defined by Yarin (2006) and was studied more recently either numerically or theoretically by Roisman *et al.* (2009), Eggers *et al.* (2010) and Villermaux & Bossa (2011). Past the initial deformation where the drop decelerates from U to zero over a characteristic length R, pressure gradients quickly vanish over a time τ so that at larger times the slender-slope Euler equation is

$$\frac{\partial v(r,t)}{\partial t} + v(r,t)\frac{\partial v(r,t)}{\partial r} \simeq 0. \tag{3.1}$$

One solution satisfying this equation reads

$$v^* = \frac{r^*}{t^* + \alpha}, \tag{3.2}$$

in very good agreement with experimental observations of figure 2(*b*). Moreover, numerical simulations performed by Roisman *et al.* (2009) and Eggers *et al.* (2010) predict the pressure-gradient-free regime, and the time offset in the above velocity field, to be of order R/U as obtained from the present data, where the delay is equal to τ, setting $\alpha = 1$.

Then, by considering mass conservation together with (3.1), the lamella thickness evolution can be deduced analytically as performed by Roisman *et al.* (2009) and Eggers *et al.* (2010). Simply, (3.1) ensures that material fluid elements move at constant radial velocity so that introducing $h^*_{ref.}(r^*)$, the initial lamella profile for which the flow field reads $v^* = r^*/\alpha$ (equation (3.2)), the latter stage advected lamella profile reads as follows:

$$h^*(r^*, t^*) = \frac{\alpha^2}{(t^* + \alpha)^2} h^*_{ref.}\left(\frac{r^*\alpha}{t^* + \alpha}\right). \tag{3.3}$$

This predicts a power-law decay for the central thickness $h_c^* = h_{ref.}(0)\alpha^2/(t^* + \alpha)^2$ in full agreement with the experimental observations. Adjusting all data with theoretical prediction yields $h_{ref.}(0) = 3.19$. This is in quantitative agreement with numerical results for inviscid flow ($h_{ref.}(0) = 2.19$; see Eggers *et al.* 2010), but in contradiction with an alternative prediction (Villermaux & Bossa 2011), where an ansatz for $h(r, t)$ inspired by a liquid jet impacting on a solid yields $h^*(r^*, t^*) \propto 1/(r^* t^*)$. Moreover, equation (3.3) predicts a self-similar profile, evidenced numerically by Roisman *et al.* (2009) and Eggers *et al.* (2010) and to a certain extent experimentally by Lagubeau *et al.* (2012) where it is partially hindered by a boundary-layer effect, as described in the next section. By measuring the whole profile with our dye absorption method, this self-similarity is recovered as reported in figure 3(*b*). In semi-quantitative agreement with the numerical estimates of Eggers *et al.* (2010), a fit of our experimental data allows us to determine $h_{ref.}$ as

$$h^*_{ref.}(x) \simeq \frac{3.19}{(1 + Cx^2)^6} \tag{3.4}$$

with $x = r^*/(t^* + 1)$ and $C = 0.604$ compared with 0.625 in the numerical predictions. The lamella thinning reported here is limited at longer time by two mechanisms. First the drop spreading and rim advance is stopped by capillary forces, before stored surface energy is recovered and a drop recoil and bounce are observed (Chandra & Avedisian 1991; Biance *et al.* 2006). At higher velocities, the lamella has time to become thin enough that spontaneous rupture occurs before recoil, through hole nucleation at the centre (Biance, Pirat & Ybert 2011).

An alternative probe of local thickness measurements is the study of a triggered hole opening dynamics in the lamella. To achieve this situation, we use a set-up previously described by Biance *et al.* (2011) where a single defect induces lamella rupture. Snapshots of an impacting drop on this surface are reported in figure 4(*a*). One can observe the shape and velocity of the hole propagating in the lamella. Its shape is well fitted by a circle whose radius r is reported versus time in figure 4(*b*). The variations of r with time follows a parabolic law and if fitted by $r(t) = a_0(t - t_h)^2 + V_0(t - t_0)$ allows the determination of the initial hole opening velocity V_0. It is expected to follow the inertial hole opening velocity given by Taylor (1959) and Culick (1960) $V_0 = \sqrt{2\gamma/\rho h}$ if h is the thickness of the lamella, whereas the parabolic contribution accounts for lamella thickness variations versus time. We deduce from this fit that the initial velocity of hole opening for an isopropanol impacting drop ($R = 1.15$ mm, $U = 2.2$ m s^{-1}) on a defect of height $h = 0.202$ mm is 0.6 ± 0.05 m s^{-1} if the rupture takes place at a time $t_0 = 2.05$ ms after the drop touches the substrate. This velocity corresponds to a thickness of 159 ± 20 μm, in very good agreement with the thickness of 168 μm expected from (3.3) and from absorption measurements under the same conditions.

3.2. *Towards global dynamics*

The local description of liquid flow during Leidenfrost impact is a starting point for building models at a more global scale. As an example, we focus here on the spreading of an impacting drop and in particular on the maximal diameter reached during impact. The global rim dynamics can be predicted along previous lines (Roisman, Rioboo & Tropea 2002; Eggers *et al.* 2010; Villermaux & Bossa 2011) building from our experimental determination of the local dynamics. The rim position

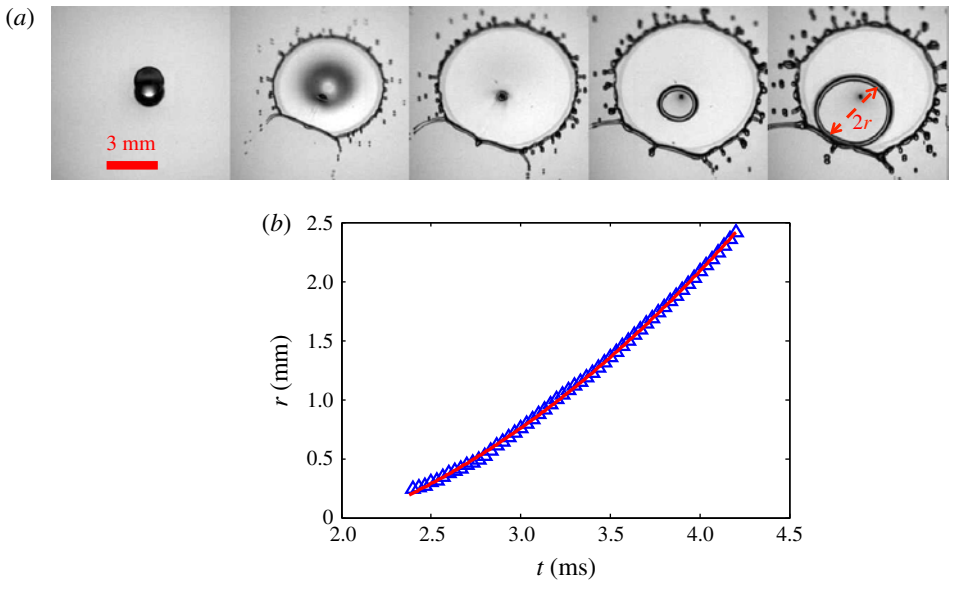

FIGURE 4. (Colour online) (*a*) Snapshots of an isopropanol droplet ($R = 1.15$ mm, $U = 2.2$ m s^{-1}) impacting on a heated solid substrate with a defect of height $h = 0.202$ mm. Lamella rupture on the defect is observed. (*b*) Variations of the hole opening radius versus time under the same conditions. The straight line corresponds to a parabolic fit (see the text) with $a_0 = 219$ m s^{-2}, $V_0 = 0.6$ m s^{-1} and $t_0 = 2.09$ ms.

and volume are noted r_m and Ω, respectively. The rim momentum variations in the inviscid limit are balanced with capillary forces which reads in dimensionless form

$$We(\ddot{r}^*_m \Omega^* + \dot{r}^*_m \dot{\Omega}^* - 2\pi r^*_m h^*(v^* - \dot{r}^*_m)v^*) = -4\pi r^*_m \tag{3.5}$$

where r_m is the rim location, h and v the thickness and velocity, respectively, of the lamella in the vicinity of the rim and given by (3.3) and (3.2), respectively.

This equation associated with rim mass conservation $\dot{\Omega}^* = 2\pi r^*_m h^*(v^* - \dot{r}^*_m)$ is numerically solved to predict rim temporal evolution for various Weber numbers. Several initial conditions, taken at $t^* = 1$, are required to solve this equation. The choice of initial conditions relies on geometric and physical self-consistent analysis and differ from previous modelling (Eggers *et al.* 2010). First, the initial rim volume is given by mass conservation integrating lamella volume using (3.3) and subtracting it to initial drop volume. The velocity of the liquid entering the rim can be determined by matching with an initial regime where the drop remains spherical and keeps a falling velocity U, and its contact diameter is given by a geometrical perturbation yielding $r_m \sim \sqrt{t}$, in good agreement with previous experimental observations (Rioboo, Marengo & Tropea 2002; Xu *et al.* 2005). The initial velocity derived from this relationship depends on the initial radius r^* with $\dot{r}^* = r^*/2$. This relationship also matches the velocity profile derived in the lamella in (3.2) for $t^* = 1$. Moreover, by analogy with jet impact on a target (Villermaux & Bossa 2011), we expect this velocity not to exceed the drop velocity. Then, for determining rim dynamics, the initial velocity is then taken as $v^*(r^*, t^* = 1) = min(r^*/2, 1)$. To close the problem, a condition on the radius of the lamella r^* at $t^* = 1$ must be determined. As predicted by

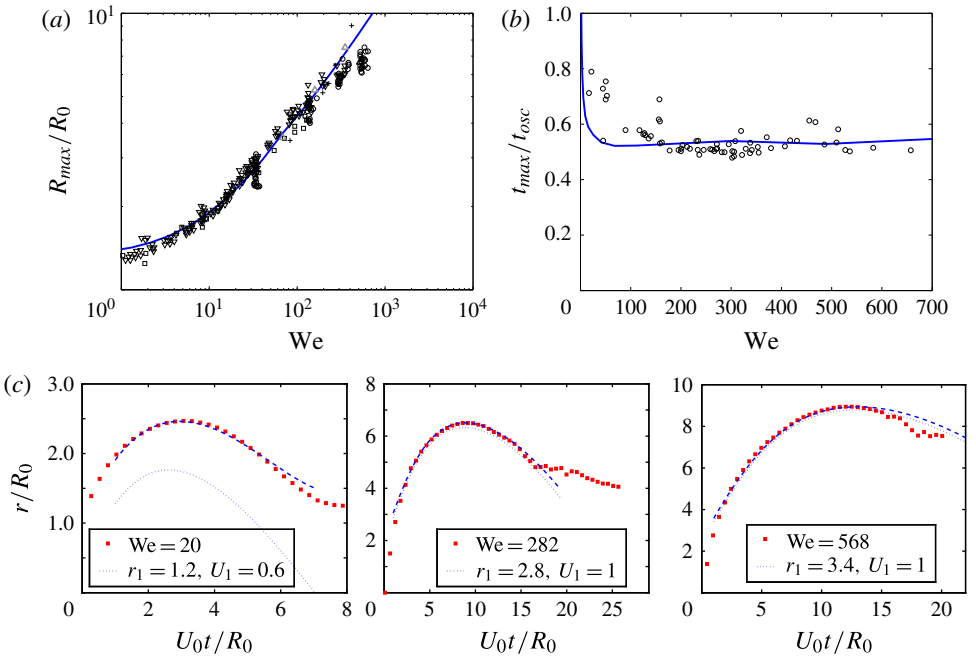

FIGURE 5. (Colour online) (*a*) Maximal dimensionless radius reached during the impact versus Weber number in log–log coordinates for various situations: (●) top view (present experiments) and (+) side view (Tran *et al.* 2012) impacts on superheated surfaces; (□) impacts on superhydrophobic surfaces (Clanet *et al.* 2004); (◇) impacts on a small target (Villermaux & Bossa 2011); (△) binary collisions (Willis & Orme 2003). (*b*) Time to reach the maximal diameter as a function of Weber number. (*c*) Rim dynamics versus dimensionless time for millimetric isopropanol droplet, corresponding to $We = 20, 282, 568$. Solid lines in (*a–c*) correspond to numerical solutions of (3.5) with appropriate initial conditions (see the text).

Eggers *et al.* (2010), the impact is divided into two stages, a first deceleration phase followed by the free pressure convective flow described previously. The establishment of this pressure-free flow occurs on the timescale $t^* = 1$. The radius reached by the drop during this step can be determined by scaling analysis. The drop falling at U is decelerated and thus submitted to an effective acceleration $g' \sim U/\tau$. If we consider that the drop adopts a quasi-static shape, it would be analogous of a puddle of height $h \sim \sqrt{\gamma/\rho g'}$ and by volume conservation, the extension reached by the drop is $r^* \sim We^{1/4}$. This prediction is in good agreement with observations (not shown here), the prefactor being set to 0.69 to fit experimental measurements. Note that a similar scaling law was derived by Clanet *et al.* (2004) to determine the maximal spreading of the drop during impact. It seems to be more adequate to introduce it in the initial stage when the pressure gradient is vanishing.

With these initial conditions, the spreading and recoiling dynamics is quantitatively well described by our numerical solving as reported in figure 5, the outer radius of the rim r_{rim} being computed by assuming a semi-toric shape of the rim and applying volume conservation. The maximal spreading radius R^*_{max} deduced from rim dynamics is reported in figure 5(*a*) and compares favourably with our experimental top-view observations. When facing the presence of fingers that alter the rim circularity, rim

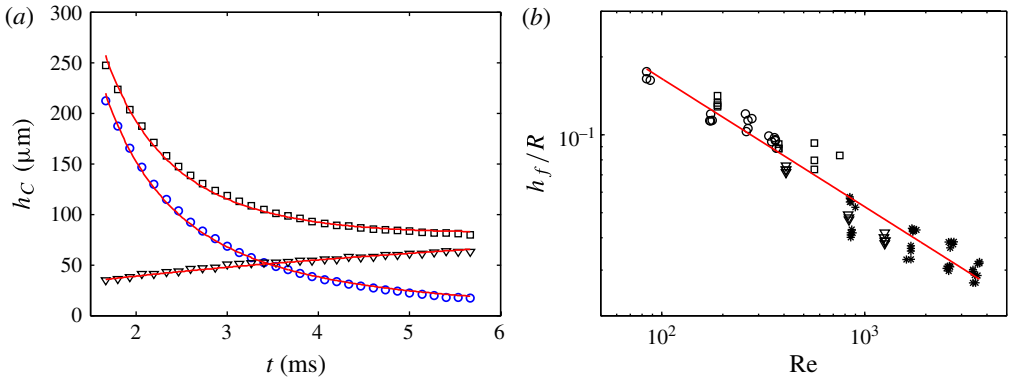

FIGURE 6. (Colour online) (*a*) Time evolution of the central thickness for both cold impact (□) and Leidenfrost impact (○). Experimental data are fitted by (3.3) for Leidenfrost impact, with $h_{add} = h - h_v$ for cold impact, and with $h_{add} = 0.49(((t^* + 1)/Re))^{0.5}$ for the difference (▽). For both experiments, $R = 1.2$ mm, $U = 2.9$ m s^{-1} and the liquid used is isopropanol, $\nu = 3.02$ mm^2 s^{-1}. (*b*) Dimensionless final thickness h_v/R versus Re in a log–log plot in the case of cold impacts for various R, U and ν (○, 12.9 mm^2 s^{-1}; □, 6.0 mm^2 s^{-1}; ▽, 2.8 mm^2 s^{-1}; ●, 12.9 mm^2 s^{-1}). The straight lines correspond to the fit $h_v/R = 0.93Re^{-2/5}$.

location refers to position of the rim edge in between fingers. Data from the literature on side-view Leidenfrost impacts have also been reported (Tran *et al.* 2012), as well as values on a small target (Villermaux & Bossa 2011) or for binary collisions (Willis & Orme 2003) where friction should be totally negligible. In addition, data on superhydrophobic surfaces (Clanet *et al.* 2004), an intermediate between air suspended spreading and solid mediated friction, are included in figure 5(*a*). Our modelling is in satisfying agreement with most of the data, and discrepancy remains within data scattering. Note that the results obtained both experimentally and theoretically do not follow a rigorous scaling law. The other global parameter which is well satisfied by our resolution is the time to reach the maximal diameter. Experimental results compare quantitatively with our prediction. Indeed, at large Weber number (above 50), this time appears independent of impact velocity and scales as the inertial capillary time $\tau_{osc} = \sqrt{(\rho R^3)/\gamma}$. The global dynamics is also well recovered for various Weber numbers as shown in figure 5(*c*).

4. Cold impacts

Building from the previous model situation of Leidenfrost impacts, which allows one to fully characterize the drop dynamics in the inviscid limit, it is possible to progress to more complex situations, e.g. when a viscous boundary layer can develop in the vicinity of the surface due to actual solid–liquid contact. Figure 1(*a*,*b*) show the impact dynamics for superheated and room temperature surfaces, respectively. Distinct differences are clearly observed while impact characteristics are the same. The central thickness versus time is reported for both situations in figure 6. While closely resembling the Leidenfrost impact at early time, the thickness in the room temperature case progressively departs from previous behaviour and eventually saturates at long times. This difference, accessed experimentally without any model assumption, has been attributed by Roisman (2009), Eggers *et al.* (2010) and Schroll *et al.* (2010)

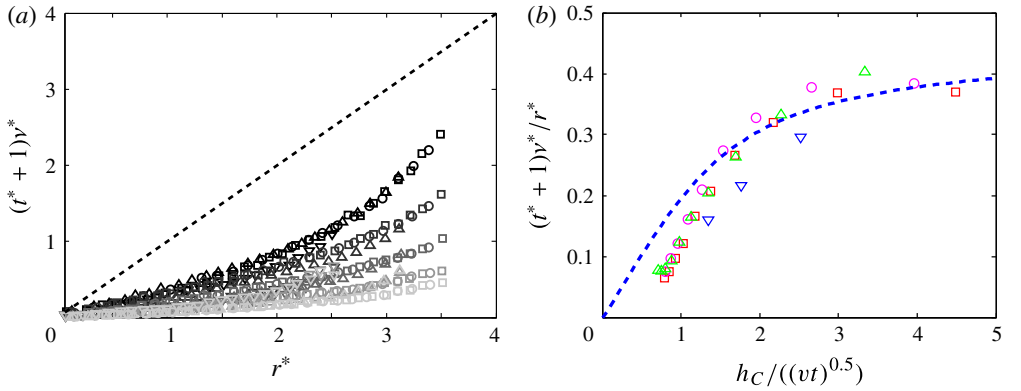

FIGURE 7. (Colour online) (*a*) Normalized velocity v^* times normalized time (t^*+1) as a function of the position in the radial coordinate in the drop ($r^* = r/R$) at different times from dark to bright ($t^* = 4$, $t^* = 6$, $t^* = 8$, $t^* = 10$ and $t^* = 12$) and different impact velocities (□, $U = 4$ m s^{-1}; ○, $U = 3$ m s^{-1}; △, $U = 2$ m s^{-1}; ▽, $U = 1$ m s^{-1}) for cold ethanol drop impacts with $R = 1.2$ mm. (*b*) Self-similar correction of velocity profile for cold impacts. Measurements are performed with an ethanol drop of initial radius $R = 1.2$ mm and various initial velocities: ▽, $U = 1$m s^{-1}; △ $U = 2$ m s^{-1}; ○, $U = 3$ m s^{-1}; □, $U = 4$ m s^{-1}; dashed line, theoretical profile given by $Cg(x)$ in the boundary layer defined by (4.1) with $C = 0.45$.

to the growth of a viscous boundary layer merging from the substrate and resulting in an extra contribution that adds to the inviscid limit: $h_{add} \propto \sqrt{\nu t}$. Using the previous results for the inviscid contribution, the additional observed thickness extracted experimentally is fitted as $\delta\sqrt{(t^*+\alpha)/Re}$, yielding $\delta = 0.49$, in excellent agreement with numerical results (Roisman 2009; Eggers *et al.* 2010) and very recent experiments (Lagubeau *et al.* 2012). In addition, this analysis predicts that the saturation thickness is reached at the merging between viscous boundary layer and unperturbed inviscid lamella thickness. This occurs at $t^*_{sat} \simeq Re^{1/5}$ showing that the final thickness varies as $h^*_f \simeq Re^{-2/5}$ (Roisman 2009; Eggers *et al.* 2010; Schroll *et al.* 2010). Such a behaviour is well recovered here as reported in figure 6(*b*) even quantitatively with similar prefactor 0.93 observed versus 1.20 predicted numerically by Bakshi, Roisman & Tropea (2007) and Roisman (2009).

The liquid velocity inside the lamella is also affected by the development of this boundary layer. In order to probe this effect, we perform PIV measurements within the drop in the case of cold impacts. A linear radial behaviour is still almost recovered as depicted in figure 7(*a*), but with a slope which depends on time and viscosity. As the velocity profile is expected to be affected only by the boundary-layer development, this slope should only depend on a single parameter which is $z/\sqrt{\nu t}$, z being the altitude in the lamella. In figure 7(*b*) we report the slope extracted from figure 7(*a*) for different impact velocities and times as a function of $h_c/\sqrt{\nu t}$, with h_c being the central thickness of the lamella. A good collapse of the data is observed. The effect of the boundary-layer development on the velocity profile within the lamella has been analytically predicted in the asymptotic regime of large $h_c/2\sqrt{\nu t}$ by Roisman (2009). As our velocity profile measurements are averaged across the lamella thickness, we integrate numerically the correction given at each altitude, and

the velocity perturbation g reads as follows:

$$g\left(\frac{h_c}{\sqrt{\nu t}}\right)=\frac{\sqrt{\nu t}}{h_c}\int_0^{(h_c)/(\sqrt{\nu t})} 1-0.54\exp(1.25x-1.2x^2)H_{-7/5}\,(1.12x-0.56)\,\mathrm{d}x \quad (4.1)$$

with $H_n(x)$ the Hermite polynomial of order n. This function is in satisfying semi-quantitative agreement with our experimental data, as reported in figure 7(*b*) where experiments match theoretical expectations up to a numerical factor C of the order of one ($C=0.45$). However, such predictions arise from asymptotic developments which is only approached especially for large boundary layers. Overall, we experimentally capture velocity profiles deviations in the case of frictional impact due to boundary-layer development, showing semi-quantitative agreement with proposed theory.

5. Conclusion

To conclude, we develop new experimental methods (dye adsorption and PIV) to probe the flow field during the impact of a drop on a solid substrate. By performing these experiments for Leidenfrost impacts, it has been possible to characterize the impact dynamics when almost no viscous coupling between the drop and the substrate occurs. In this case, the experimental results are well described by an advecting plug flow within the drop lamella. We use these new insights in the description of drop impact for complete prediction of maximal extension in the ideal frictionless case. This local description is also a crucial point for further studies where, for instance, the coupling between drop and substrate must be taken into account. For example, the frictional coupling results in the formation of a viscous boundary layer from the substrate as previously predicted (Roisman 2009; Eggers *et al.* 2010; Lagubeau *et al.* 2012). Moreover, a comparison between these two extreme cases allows us to evidence directly the boundary-layer development. These new results constitute a starting point for developing new models aiming at describing the complex phenomenon of drop impact and for example predicting splash mechanism.

Acknowledgements

The authors would like to thank ANR for funding through the FREEFLOW project (contract number ANR-11BS04-001-02) and Gilles Simon for technical support.

Appendix. Dye adsorption technique for thickness profile measurements

In this appendix, we describe the technique employed for thickness profile measurements, and its range of validity. The measurement is based on analysis of the intensity of the light absorbed by the drop seeded with a specific dye and its reflexion on a silica wafer. A first part aims at estimating the uncertainties due to drop shape (curvature and slope), and the second part describes light absorption and reflexion along the optical path.

Description of the experimental set-up

The set-up is described in figure 8(*a*). A white light passing through a diffuser of radius $R_s=3.6$ cm is emitted with an incident angle $\beta\simeq 20^\circ$ on the drop at a distance $Z_S-Z_D=23$ cm. The partially reflected light is collected at a specular angle through an aperture of radius $R_D=0.94$ cm on the high-speed camera CCD sensor via an objective, located at a distance $Z_D=30.7$ cm from the drop. An equivalent optical path of the drop, which when curved acts as an optical lens is schematized in figure 8(*b*).

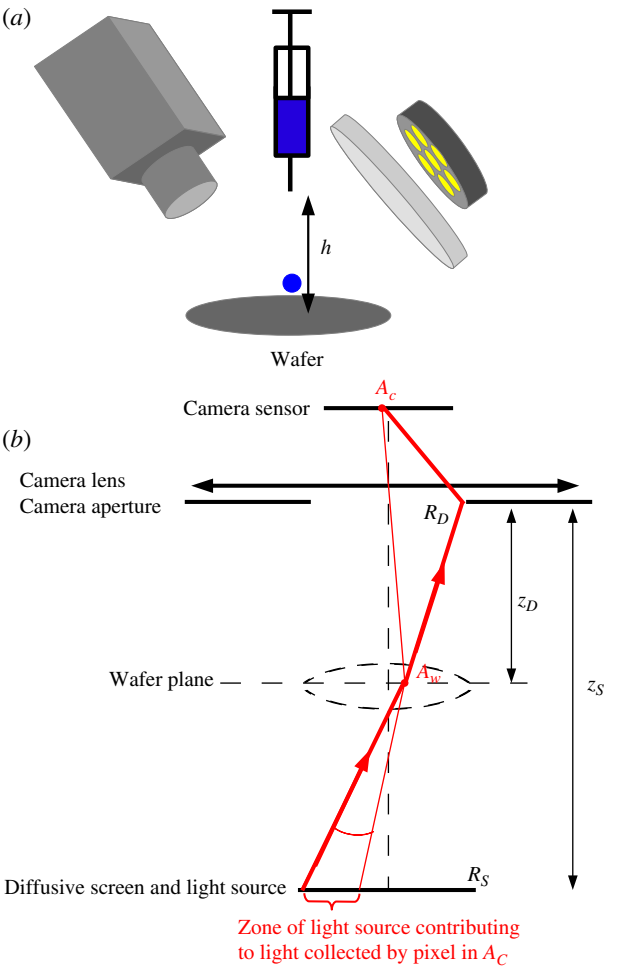

FIGURE 8. (Colour online) (*a*) Scheme of the experimental set-up showing the position of the light source and camera during an experiment. (*b*) Optical path when the spherical cap of a drop acts as a converging lens.

Effect of the interface curvature

To investigate the effect of the interface curvature, the case of a droplet having the shape of a spherical cap is considered. Owing to index differences between air and liquid, the drop acts as an optical lens, whose focal length is given by $f = (R_C)/(2(n-1))$, where R_C is the radius of curvature of the interface and n is the optical index of the liquid. The light reflected on the wafer through the drop is collected by the CCD if the light emitted by the diffuser and reflected by the wafer can pass through the camera aperture. To quantify this effect, an analogous optical path can be built by considering the light emitted by the source and passing through the image of the camera aperture by the drop acting as an optical lens. We can see that as drop curvature increases, the image of the aperture position is closer to the drop and zones on the drop border are not imaged on the CCD. This effect, illustrated in figure 9, has been verified experimentally and numerically. A criterion that gives the minimum focal length for which all of the light contributions for the illumination

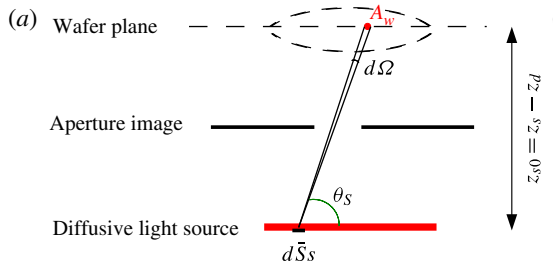

FIGURE 9. (Colour online) Effect of the aperture camera image position (which varies with drop curvature) on the light collected from a non-centred point of the drop. (*a*) Case of a small interface curvature where all of the points are observed. (*b*) Case of a high interface curvature and example of a non-collected zone.

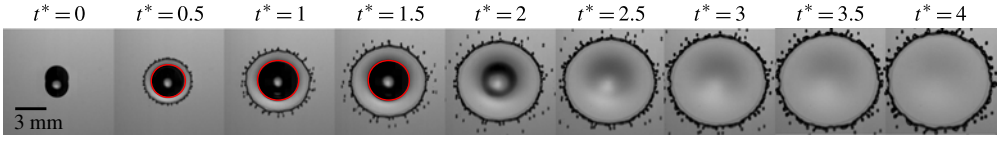

FIGURE 10. (Colour online) Snapshots of an ethanol drop ($R = 1.15$ mm, $U = 2$ m s^{-1}) impacting a heated substrate. The circles (shown in red online) corresponds to high curved zone where no light from the diffuse source can reach the camera CCD. A shaded zone remains visible until $t = 4\tau$, in good agreement with the method limitation.

of a drop of radius r_0 belong to the diffusor of radius R_S reads as follows:

$$f \geqslant \frac{z_S - z_D}{\dfrac{R_S}{r_0} - \dfrac{z_S}{z_D}}. \tag{A 1}$$

On the other hand, the maximum of curvature of the drop profile during impact is deduced from (3.3) and reads as follows:

$$R_{C,max} \simeq 0.042 \frac{(t+\tau)^4 U^4}{R^3} \tag{A 2}$$

and the typical extension of profile thickness variation is given by $r_0 \sim (t + \tau)U$. Therefore, under the experimental conditions described above, this criterion reads $t \geqslant 3.78\tau$, which corresponds to the lower limit of the experimental results presented here. To illustrate this effect, snapshots of a drop impinging on a solid surface is reported in figure 10, where indeed a dark zone is observed at short times and for high curvatures.

Effect of the interface slope

Refraction effect due to the interface slope can modify the path length of the light and therefore its attenuation by absorption. The light path on a sloppy interface is sketched in figure 11, and the uncertainty $\delta h/h$ can be estimated geometrically. Temporal evolution of $\delta h/h$ is reported in table 1 for the drop profile described by (3.3). This effect is negligible for $t \geqslant 4\tau$. Moreover, our technique has been validated

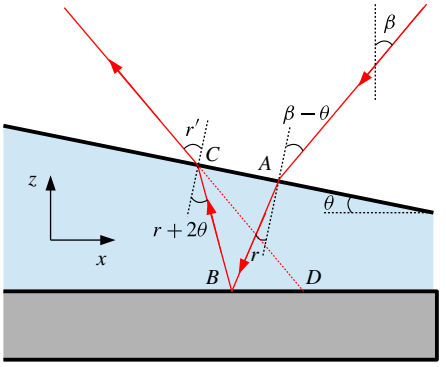

FIGURE 11. (Colour online) Geometrical scheme showing the effect of the interface slope on the length of light path through the drop.

t^*	θ_{max} (deg.)	$((\partial h)/h)$ (%)
1	35	27.3
2	10	10.5
3	4.4	4.6
4	2.3	2.4
5	1.3	1.3

TABLE 1. Evaluation of errors achieved due to the slope of the interface for thickness profile measurements.

by indirect measurements of thickness by analysing the opening dynamics of holes in the lamella as reported in figure 4.

These effects limit our experiments to times above $t > 4U/R$. As an illustration, a straight comparison of the drop profile with side-view analysis (only possible at short time when the cap is not hidden by the rim) shows a good agreement between both measurements as reported in figure 1(*f*) and confirms the validity of our experimental investigation at the shortest times explored, when the slope and curvature of the drop are maximum. Note that evaporation is not a concern at these timescales, as the evaporation rate is around 1 $mm^3\ s^{-1}$ under similar experimental conditions Biance *et al.* (2003), resulting on thickness variations below 1 nm during the impact process, largely below our thickness resolution.

Light attenuation and calibration

After checking the linearity of the camera CCD sensor, we calibrate our measurement set-up by studying light collected after crossing pools of varying height h filled with dye at a given concentration. The light intensity collected is well fitted by the relation:

$$g(h) = g_0 + g_1 \exp(-\alpha h). \tag{A 3}$$

This relationship is then inverted in real experiments to determine the thickness h the light has crossed. Here g_0 and g_1 depend on Fresnel coefficients expected for transmission and reflexion on a liquid/gas and liquid/wafer interface. To validate our

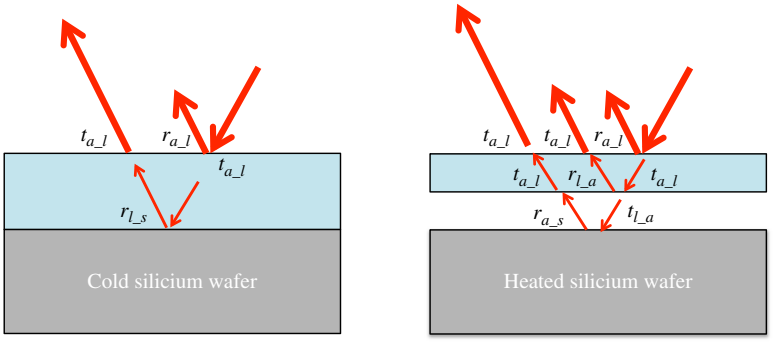

FIGURE 12. (Colour online) Light path on a cold substrate and on a heated substrate, showing the reflexion and transmission coefficients taken into account in both cases.

measurements accuracy, the light collected by reflexion on the wafer g_2 has also been evaluated, and we verified the following relationships:

$$\frac{g_0}{g_2} = \frac{r_{a-l}}{r_{a-s}} \quad \text{and} \quad \frac{g_1}{g_2} = \frac{t_{a-l}^2 r_{l-s}}{r_{a-s}} \tag{A 4}$$

where r_{i-j} and t_{i-j} are the respective reflexion and transmission optical coefficient on the interface $i-j$.

In the case of Leidenfrost impact, a different attenuation relationship is used, taking into account reflexion and transmission through a interstitial air layer as reported in figure 12, the new coefficients satisfying

$$\frac{g_1'}{g_2} = t_{a-l}^4 \quad \text{and} \quad \frac{g_1'}{g_1} = \frac{t_{a-l}^2 r_{a-s}}{r_{l-s}}. \tag{A 5}$$

REFERENCES

BAKSHI, S., ROISMAN, I. V. & TROPEA, C. 2007 Investigations on the impact of a drop onto a small spherical target. *Phys. Fluids* **19** (3), 032102.

BIANCE, A. L., CHEVY, F., CLANET, C., LAGUBEAU, G. & QUERE, D. 2006 On the elasticity of an inertial liquid shock. *J. Fluid Mech.* **554**, 47–66.

BIANCE, A. L., CLANET, C. & QUERE, D. 2003 Leidenfrost drops. *Phys. Fluids* **15** (6), 1632–1636.

BIANCE, A. L., PIRAT, C. & YBERT, C. 2011 Drop fragmentation due to hole formation during leidenfrost impact. *Phys. Fluids* **23** (2), 022104.

BUSSMANN, M., CHANDRA, S. & MOSTAGHIMI, J. 2000 Modeling the splash of a droplet impacting a solid surface. *Phys. Fluids* **12**, 3121–3132.

CHANDRA, S. & AVEDISIAN, C. T. 1991 On the collision of a droplet with a solid surface. *Proc. R. Soc. Lond.* A **432**, 13–41.

CLANET, C., BEGUIN, C., RICHARD, D. & QUERE, D. 2004 Maximal deformation of an impacting drop. *J. Fluid Mech.* **517**, 199–208.

CULICK, F. 1960 Comments on a ruptured soap film. *J. Appl. Phys.* **31**, 1128–1129.

DE RUITER, J., OH, J. M., VAN DEN ENDE, D. & MUGELE, F. 2012 Dynamics of collapse of air films in drop impact. *Phys. Rev. Lett.* **108**, 074505.

DRISCOLL, M. M. & NAGEL, S. R. 2011 Ultrafast interference imaging of air in splashing dynamics. *Phys. Rev. Lett.* **107**, 154502.

EGGERS, J., FONTELOS, M. A., JOSSERAND, C. & ZALESKI, S. 2010 Drop dynamics after impact on a solid wall: theory and simulations. *Phys. Fluids* **22**, 062101.

KOLINSKI, J. M., RUBINSTEIN, S. M., MANDRE, S., BRENNER, M. P., WEITZ, D. A. & MAHADEVAN, L. 2012 Skating on a film of air: drops impacting on a surface. *Phys. Rev. Lett.* **108**, 074503.

LAGUBEAU, G., FONTELOS, M. A., JOSSERAND, C., MAUREL, A., PAGNEUX, V. & PETITJEANS, P. 2012 Spreading dynamics of drop impacts. *J. Fluid Mech.* **713**, 50–60.

LATKA, A., STRANDBURG-PESHKIN, A., DRISCOLL, M. M., STEVENS, C. S. & NAGEL, S. R. 2012 Creation of prompt and thin-sheet splashing by varying surface roughness or increasing air pressure. *Phys. Rev. Lett.* **109**, 054501.

MANDRE, S., MANI, M. & BRENNER, M. P. 2009 Precursors to splashing of liquid droplets on a solid surface. *Phys. Rev. Lett.* **102**, 134502.

RANGE, K. & FEUILLEBOIS, F. 1998 Influence of surface roughness on liquid drop impact. *J. Colloid Interface Sci.* **203**, 16–30.

RICHARD, D., CLANET, C. & QUERE, D. 2002 Surface phenomena—contact time of a bouncing drop. *Nature* **417**, 811.

RIOBOO, R., MARENGO, M. & TROPEA, C. 2002 Time evolution of liquid drop impact onto solid, dry surfaces. *Exp. Fluids* **33**, 112–124.

ROISMAN, I. V. 2009 Inertia dominated drop collisions. II. An analytical solution of the Navier–Stokes equations for a spreading viscous film. *Phys. Fluids* **21** (5), 052104.

ROISMAN, I. V., BERBEROVIC, E. & TROPEA, C. 2009 Inertia dominated drop collisions. I. On the universal flow in the lamella. *Phys. Fluids* **21**, 052103.

ROISMAN, ILIA. V., RIOBOO, R. & TROPEA, C. 2002 Normal impact of a liquid drop on a dry surface: model for spreading and receding. *Proc. R. Soc. Lond.* A **458** (2022), 1411–1430.

SCHROLL, R. D., JOSSERAND, C., ZALESKI, S. & ZHANG, W. W. 2010 Impact of a viscous liquid drop. *Phys. Rev. Lett.* **104**, 034504.

TAYLOR, G. I. 1959 The dynamics of thin sheets of fluid. 3. Disintegration of fluid sheets. *Proc. R. Soc.* A **253**, 313–321.

TRAN, T., STAAT, H. J. J., PROSPERETTI, A., SUN, C. & LOHSE, D. 2012 Drop impact on superheated surfaces. *Phys. Rev. Lett.* **108**, 036101.

VAN DER VEEN, R. C. A., TRAN, T., LOHSE, D. & SUN, C. 2012 Direct measurements of air layer profiles under impacting droplets using high-speed color interferometry. *Phys. Rev.* E **85**, 026315.

VILLERMAUX, E. & BOSSA, B. 2011 Drop fragmentation on impact. *J. Fluid Mech.* **668**, 412–435.

WACHTERS, L. H. & WESTERLING, N. A. 1966 Heat transfer from a hot wall to impinging water drops in spheroidal state. *Chem. Engng Sci.* **21**, 1047–1056.

WILLIS, K. & ORME, M. 2003 Binary droplet collisions in a vacuum environment: an experimental investigation of the role of viscosity. *Exp. Fluids* **34**, 28–41.

WORTHINGTON, A. M. 1876 On the form assumed by drops of liquids falling vertically on horizontal plate. *Proc. R. Soc.* **25**, 261–271.

XU, L. 2007 Liquid drop splashing on smooth, rough, and textured surfaces. *Phys. Rev.* E **75**, 056316.

XU, L., ZHANG, W. W. & NAGEL, S. R. 2005 Drop splashing on a dry smooth surface. *Phys. Rev. Lett.* **94**, 184505.

YARIN, A. L. 2006 Drop impact dynamics: splashing, spreading, receding, bouncing. . . . *Annu. Rev. Fluid Mech.* **38**, 159–192.